Journal of Catalysis **205,** 309–317 (2002)
doi:10.1006/jcat.2001.3441, available online at http://www.idealibrary.com on IDEAL®

Methane Combustion and CO Oxidation on Zirconia-Supported La, Mn Oxides and $LaMnO_3$ Perovskite

S. Cimino,* S. Colonna,† S. De Rossi,‡ M. Faticanti,‡ L. Lisi,§ I. Pettiti,‡ and P. Porta‡,[1]

*Dipartimento d'Ingegneria Chimica, Università "Federico II," Napoli, Italy; †Istituto di Struttura della Materia, CNR, Via Fosso del Cavaliere 100, 00133 Roma, Italy; ‡Centro di Studio "Struttura e Attività Catalitica di Sistemi di Ossidi," CNR, c/o Dipartimento di Chimica, Università degli Studi di Roma "La Sapienza," Piazzale Aldo Moro 5, 00185 Roma, Italy; and §Istituto di Ricerche sulla Combustione, CNR, c/o Dipartimento d'Ingegneria Chimica, Piazzale V. Tecchio 80, 80125 Napoli, Italy

Received June 8, 2001; revised September 24, 2001; accepted September 24, 2001

ZrO_2-supported La, Mn oxide catalysts with different La, Mn loading (0.7, 2, 4, 6, 12, and 16 wt% as $LaMnO_3$) were prepared by impregnation of tetragonal ZrO_2 with equimolar amounts of La and Mn citrate precursors and calcination at 1073 K. The catalysts were characterized by X-ray diffraction (XRD), X-ray absorption spectroscopy (XAS), and BET specific surface area determination. The redox properties were tested by temperature-programmed reduction (TPR), and the catalytic tests were carried out for methane combustion at 650–1050 K and for CO oxidation at 350–800 K. XRD revealed the presence of tetragonal zirconia with traces of the monoclinic phase. $LaMnO_3$ perovskite was also detected for loading higher than 6%. XAS and TPR experiments suggested that at high loading small crystallites of $LaMnO_3$, not uniformly spread on the zirconia surface, were formed; while at low loading, La, Mn oxide species interacting with the support, and hard to be structurally defined, prevailed. The catalysis study indicated that the presence of a perovskite-like structure is necessary for the development of highly active sites. Dilute catalysts were in fact poorly active even when considering the activity per gram of La, Mn perovskite-like composition. For methane combustion and CO oxidation, similar trends of the activity as a function of the loading point to a similarity of the active sites for the two reactions on the examined catalytic system.

Key Words: **zirconia-supported La, Mn perovskites; redox properties; methane combustion; CO oxidation.**

1. INTRODUCTION

Oxides with a perovskite structure (ABO_3) and containing transition metal ions have attracted considerable interest for many years due to their activity and thermal stability in the catalytic total oxidation of hydrocarbons (1–3). In particular, the catalytic combustion of methane represents a promising way for power generation to avoid the formation of harmful nitrogen oxides (NO_x), which are otherwise produced at the high temperatures of the flame combustion (4, 5).

A great variety of metal ions can be introduced in the perovskite structure provided that their ionic radii fit the sizes of the 12 coordinated A and octahedral B sites, e.g., $r_A > 0.90$ Å and $r_B > 0.51$ Å. Moreover, various oxidation states of the A and B cations are allowed in the perovskite structure as well as anionic or cationic defectivity (5–8). Therefore, the ABO_3 perovskite can be considered an ideal host matrix for many transition or nontransition metal ion solid solutions.

One of the main drawbacks of the perovskites is their very low surface area (some square meters per gram) when they are prepared by solid-state reaction of the oxide precursors at high temperature (5, 8). Although a method based on citrates precursors (9) allows the production of perovskites even with a few tens of square meters per gram of specific surface area after calcination at 1073 K (10–13), rapid sintering at temperatures such as 1173 K cannot be avoided. Therefore, dispersion of perovskites on suitable high surface area refractory supports could increase the specific activity and thermal resistance of these catalysts. Among the proposed supports, γ-Al_2O_3 is the most widely investigated (14–18), due to its high surface area and thermal stability when doped with superficial La_2O_3. Nevertheless, interactions occurring between active phase and support result in the formation of mixed perovskites or in the inclusion of transition metal ions in the alumina lattice, which reduce the activity of the catalyst (15–18). Interactions between Mg^{2+} ions and $LaMnO_3$ have also been reported when magnesia is used as a support (18). ZrO_2 could represent a good support, since it should give moderate interactions with perovskite. Fujii *et al.* and Mizuno *et al.* (19, 20) found that the specific activity of supported $LaCoO_3$ and $La_{0.8}Sr_{0.2}CoO_3$ perovskites in the oxidation of propane was significantly enhanced only through the dispersion of a few layers on ZrO_2.

This paper reports the results concerning the preparation, characterization, and catalytic activity for methane combustion of La, Mn oxides dispersed on high surface area tetragonal ZrO_2. In fact, $LaMnO_3$ perovskite was found to be one of the most active catalysts for the total oxidation

[1] To whom correspondence should be addressed. Fax: 39 06 490324. E-mail: piero.porta@uniroma1.it.

0021-9517/02 $35.00

of methane (5, 10, 12). CO oxidation was also investigated to have information on the catalytic properties toward oxidation in a lower temperature range compared to that in which methane oxidation takes place (13).

2. EXPERIMENTAL

La, Mn oxides/ZrO_2 catalysts with different La–Mn loading (hereafter designated as ZLaMn with the number after the label indicating the nominal perovskite content: 0.7, 2, 4, 6, 12, and 16 wt%) were prepared by impregnation of tetragonal ZrO_2 with equimolar amounts of citrate precursors.

Tetragonal ZrO_2 with a large surface area was prepared by the method of Chuah *et al*. (21). An aqueous solution of 0.075 M $ZrOCl_2$ was added, dropwise (1 mL min^{-1}) and under magnetic stirring, to a 5 M NH_4OH solution. The hydrous zirconia, after digestion in its mother solution at 373 K for 48 h, was filtered, washed with water until the $AgNO_3$ test for Cl^- detection gave no opalescence in the washing solution, dried in a furnace overnight at 383 K, and finally calcined at 1073 K for 5 h (raising the temperature slowly by 1 K min^{-1}).

The dispersion of La, Mn oxides on the ZrO_2 support was performed by the citrate method (9, 15). Two solutions were added to a weighted amount of ZrO_2: an aqueous solution of citric acid was added first, and subsequently a solution containing $La(NO_3)_3$ and $Mn(NO_3)_2$ in 1 : 1 proportions was added. The molar ratio between the citric acid and the overall metal nitrates was fixed at 1. The resulting solution was kept at 383 K until dryness, and the samples, after grinding, were calcined at 1073 K for 5 h. For comparison, unsupported $LaMnO_3$ was also prepared by the citrate method as reported in (11).

The BET surface area of samples (SA, $m^2\ g^{-1}$) was evaluated by nitrogen adsorption at 77 K in a vacuum glass apparatus.

Phase analysis was performed by X-ray powder diffraction using a Philips PW 1029 diffractometer with Ni-filtered Cu$K\alpha$ radiation. Spectra were recorded in a 2ϑ range from 20 to 60°.

X-ray absorption spectroscopy (XAS) measurements of some ZLaMn materials (2, 6, and 12% loading) and of pure $LaMnO_3$ were performed at the ESRF Italian beamline GILDA (Grenoble, France). Mn and La K-edges were measured at 77 K in a fluorescence detection mode using a high purity Ge detector for the ZLaMn samples and in a transmission mode for $LaMnO_3$. Powder samples were deposited on Millipore membranes or mixed to an appropriate amount of boron nitride (BN) and pressed into pellets. The beamline monochromator was equipped with two Si (311) crystals for Mn K-edge measurements and two Si (511) crystals for La K-edge measurements. The EXAFS analysis was performed by using the complete FEFF8 package (22). Fourier transforms (FTs) for the signal $k^3\chi(k)$ were calculated in the range $2.5 < k < 11.5$ Å^{-1} by using a Kaiser window.

Temperature-programmed reduction (TPR) experiments were performed as reported in (10) using a Micromeritics TPD/TPR 2900 analyzer equipped with a TC detector and coupled with a Hiden HPR 20 mass spectrometer. Samples (0.1 g) were preheated in flowing air at 1073 K for 2 h and then, after cooling at room temperature, reduced with a 2% H_2/Ar mixture (25 $Ncm^3\ min^{-1}$), and heated at 10 K min^{-1} up to 1073 K. Water produced by the sample reduction was condensed in a cold trap before reaching the detectors.

Methane catalytic combustion experiments were performed in the experimental apparatus already described elsewhere (13, 18). The space velocity was 40,000 $Ncm^3\ g^{-1}\ h^{-1}$ in all tests (0.4 g catalyst powder, 150–250 μm), with a feed gas composition of 0.4% CH_4, 10% O_2, and N_2 balance. Product concentrations were continuously measured after passing a $CaCl_2$ water trap by five on-line-independent nondispersive infrared analyzers for CH_4 (high and low conc.), CO, CO_2, and NO. The reproducibility of results was verified carrying out each test twice and loading fresh catalysts every time.

CO oxidation with O_2 was studied following the experimental procedure already described in (13), using 0.5 g of catalyst supported on a silica-fritted disk inside a silica reactor vertically positioned in a programmable electrical heater. The compositions of the reactants were adjusted to 1% CO, 20% O_2, and He balance, and the space velocity was 12,000 $Ncm^3\ g^{-1}\ h^{-1}$. Effluent from the reactor was sampled and analyzed by gas chromatography; mass balance with respect to carbon was 100% ± 2%.

Kinetic parameters for both reactions were evaluated under the assumption of isothermal plug flow conditions, on the basis of a first-order rate expression with respect to CH_4 or CO and a zeroth pseudo-order with respect to oxygen because it was present in large excess.

3. RESULTS AND DISCUSSION

3.1. Structural Properties

Phase analysis, performed by X-ray powder diffraction, showed that with up to 6% loading no other phase but tetragonal zirconia (with only traces of the monoclinic phase) was revealed. Figure 1 shows that in the ZLaMn-12 and ZLaMn-16 samples, in addition to the ZrO_2 X-ray diffraction (XRD) pattern, small peaks are visible. Their intensity increases with the increase of La–Mn loading, their position corresponding to that of the strongest peaks of $LaMnO_3$ perovskite.

The preparation method leads to the stabilization of ZrO_2 in its tetragonal phase characterized by a BET surface area of 82 $m^2\ g^{-1}$ even after 5 h calcination at 1073 K, making it suitable as a catalyst support. The dispersion of active

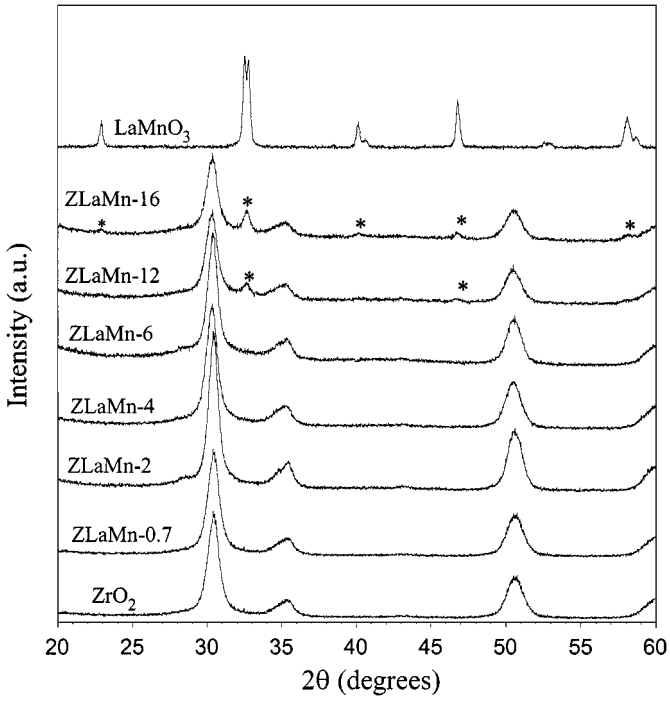

FIG. 1. XRD patterns of ZrO_2, $LaMnO_3$, and ZLaMn catalysts. Asterisks indicate the most intense X-ray lines of $LaMnO_3$.

components and the following calcination step yielded final surface areas of ZLaMn samples in the range 50–67 $m^2\ g^{-1}$. The variations of surface area values can be related to the uncontrolled small amounts of monoclinic zirconia present on the various samples.

The structural investigation on the nature of the active phase of the zirconia-supported samples was carried out by X-ray absorption spectroscopy (XAS) at the La K-edge (for ZLaMn-2, ZLaMn-6, and ZLaMn-12) and at the Mn K-edge (for ZLaMn-6 and ZLaMn-12).

Figure 2 shows the FTs of the $k^3\chi(k)$ signals, measured at the La K-edge, of the previously described catalysts and of the unsupported $LaMnO_3$ perovskite. For $LaMnO_3$ the FT shows two low intensity first shell peaks due to different La–O bond distances [2.48 and 2.75 Å, respectively, from crystallographic data (11)] and a very intense second shell peak at about 2.8 Å representing the further shells. The FTs for the ZLaMn catalysts show the presence of a broad first shell peak in the range 1.0–2.5 Å, with an intensity which decreases with the increase of La content, and second shell structures in the range 2.5–4.4 Å. These second shell features for the ZLaMn-2 and ZLaMn-6 samples are shifted to higher R values and are less intense, while ZLaMn-12 resembles pure $LaMnO_3$ with a strong second shell structure at about 2.8 Å.

The FT of pure perovskite was fitted by using the crystallographic bond distances data (11), leaving free the E_0 shift, the S_0^2 term, and the Debye–Waller factors. In the fitting procedure of the catalysts two La–O contributions were used to reproduce the near-neighbors coordination. The second shell structures were fitted using both La–Mn and La–La contributions. Debye–Waller factors and E_0 and S_0^2 parameters were fixed to the value obtained from the fit of the pure perovskite. The coordination number (N) and bond distances (R) were left to vary in the fit. The Debye–Waller factors were fixed to avoid the strong correlation with the coordination numbers. The fit results are reported in Table 1, and the fit profiles (dots) are shown in Fig. 2.

From these results it is evident that perovskite is the most abundant phase in the ZLaMn-12 sample. In fact, the distances (found equal to 3.39 and 3.92 Å for the La–Mn and La–La contributions, respectively) agree well with the expected distances for $LaMnO_3$ (3.33–3.39 and 3.89 Å, respectively). The reduced coordination numbers indicate a disorder on the surface of the support and/or the presence of small crystallites. For the ZLaMn-2 sample, the FT exhibits a different shape indicating a peculiar kind of species present on the surface. The fit results show a reduction of the La–Mn and La–La coordination numbers and a shift of the coordination distances, the La–Mn distance being greater and the La–La distance shorter than those in the perovskite structure. These results should imply the formation of

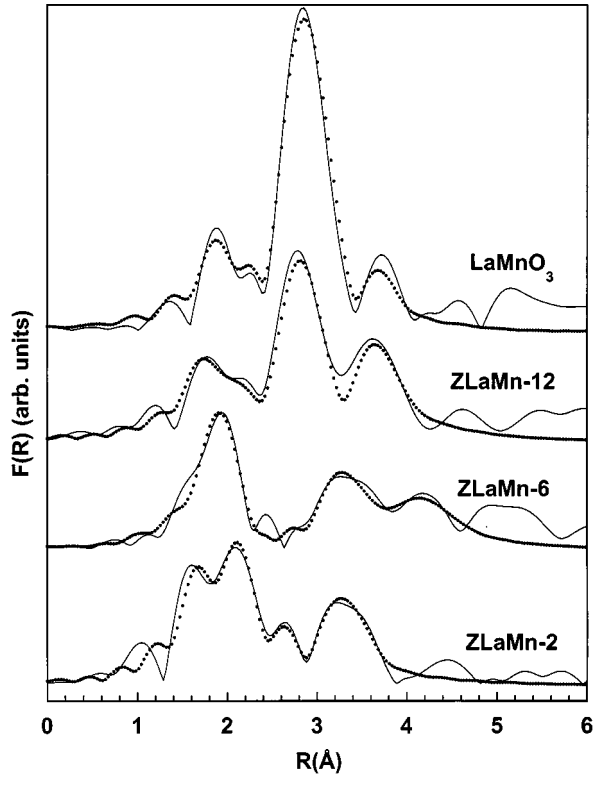

FIG. 2. La K-edge: Fourier transforms of the $k^3\chi(k)$ signals for the ZLaMn-2, ZLaMn-6, and ZLaMn-12 samples compared to pure $LaMnO_3$. The continuous line represents the experimental data, and the dots are the fit profiles.

TABLE 1

Fitting Results Obtained from the EXAFS Analysis at the La and Mn K-Edges[a]

	La K-edge					
	La–O	La–O	La–Mn	La–La	La–Mn	La–La
ZLaMn-2						
$N \pm 0.8$	3.5	4.8	1.6	2.3	—	—
R(Å) ± 0.02	2.44	2.60	3.48	3.64	—	—
ZLaMn-6						
$N \pm 0.8$	4.3	1.9	1.4	2.0	2.0	1.2
R(Å) ± 0.02	2.48	2.63	3.51	3.67	4.64	4.65
ZLaMn-12						
$N \pm 0.8$	3.2	3.3	4.6	3.8	—	—
R(Å) ± 0.02	2.42	2.60	3.39	3.92	—	—

	Mn K-edge		
	Mn–O	Mn–La	Mn–Mn
ZLaMn-6			
$N \pm 0.8$	6.2	0.8	0.9
R(Å) ± 0.03	1.92	3.42	3.87
ZLaMn-12			
$N \pm 0.8$	6.0	2.2	2.0
R(Å) ± 0.03	1.94	3.39	4.01

[a] N is the coordination number, and R is the bond distance for the different coordination shells.

extremely disordered and dispersed metal oxides on the support surface. By increasing the La–Mn loading up to 6% some differences in the FT can be observed, in particular the presence of a double peak in the second shell structure. The best fit of ZLaMn-6 was obtained using two La–La and two La–Mn contributions, as reported in Table 1. This fit reveals an increase in the total La-La and La-Mn coordination numbers pointing to a greater aggregation of the supported oxide species with respect to ZLaMn-2. The found La-La and La-Mn bond distances are different from those of the perovskite structure suggesting that a completely organized perovskite is formed only at high loading.

Figure 3 shows the FTs of the $k^3\chi(k)$ signals, measured at the Mn K–edge, of the ZLaMn-6 and ZLaMn-12 samples and of pure $LaMnO_3$. An intense first shell peak in the $R = 0.8$–2.0 Å range, which is evidently broadened for the ZLaMn-6 sample, is observed, due to Mn–O coordination. The structures in the 3–4 Å range are due to the further shells.

Fits of these spectra were performed using three different coordination shells: Mn–O, Mn–La, and Mn–Mn. Also in this case the Debye–Waller factors were fixed to the values obtained from the fit of the pure perovskite. The results are reported in Table 1, and fit profiles are shown in Fig. 3 (dots). These results confirm that the 12% sample exhibits a perovskite-type structure. In fact, the Mn–O and Mn–La distances are in agreement with the crystallographic data (1.96 and 3.37–3.39 Å, respectively). Only the Mn–Mn distance results are longer than those expected from the $LaMnO_3$ crystal structure (3.88 Å), but this is probably due to the fact that multiple scattering contributions, particularly those in the planar Mn–O–O, were neglected in this fit. As for the ZLaMn-6 sample, the FT shows a lower intensity second shell structure and a Mn–La distance close to that of pure perovskite. This suggests, in agreement with the results drawn from the La K-edge measurements, that in ZLaMn-6 the oxide dispersed on ZrO_2 is a perovskite-like structure, although not well organized as indicated by the low coordination number around Mn.

3.2. Redox Properties

The TPR profiles of the ZLaMn-supported catalysts are shown in Fig. 4, where the patterns of bulk $LaMnO_3$, MnO, Mn_3O_4, Mn_2O_3, MnO_2, and ZrO_2 are reported for comparison. The total H_2 uptake estimated from the experiments carried out up to 1073 K and that related to the first peak evaluated up to the minimum baseline value reached in the 823–923 K temperature range are reported in Table 2.

MnO displays a very small peak at 740 K probably due to the reduction of some surface manganese oxide species with a Mn oxidation state higher than 2+. The reduction temperature of the other manganese oxide reference

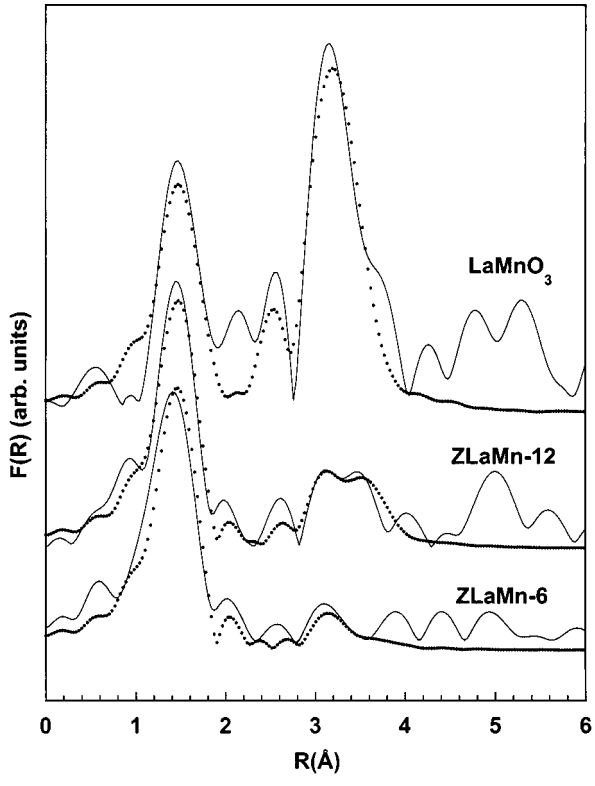

FIG. 3. Mn K-edge: Fourier transforms of the $k^3\chi(k)$ signals for the ZLaMn-6 and ZLaMn-12 samples compared to pure $LaMnO_3$. The continuous line represents the experimental data and the dots are the fit profiles.

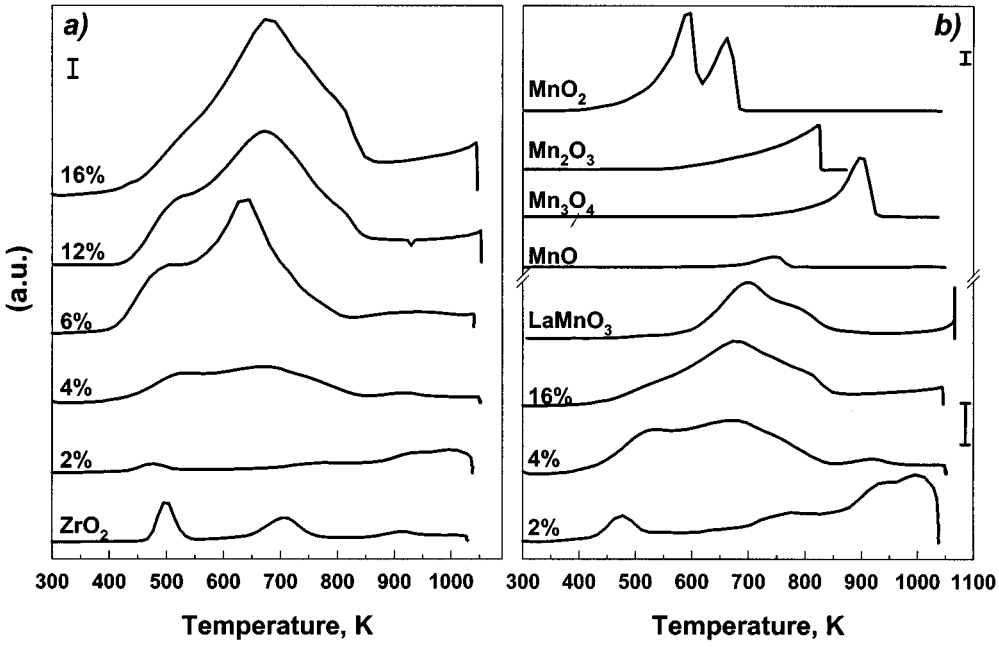

FIG. 4. TPR profiles of $LaMnO_3$-supported catalysts and reference compounds. (a) Per gram of catalyst. (b) Per mole of Mn. Bars in (a) and (b) correspond to 0.1 $\mu mol_{H_2}\ g^{-1}\ K^{-1}$ and 1 $mmol_{H_2}\ mol_{Mn}^{-1}\ K^{-1}$, respectively.

phases is, as expected, in the order of MnO_2 (two steps) < Mn_2O_3 <Mn_3O_4.

ZrO_2 shows a quite sharp signal peaked at about 490 K and a broader signal peaked at about 700 K. The first peak was assigned, by simultaneous mass spectrometry analysis, to desorption of CO_2 present as an impurity in the air used for the sample pretreatment. The second peak indicates that some reduction of ZrO_2 occurs at high temperature. Both signals undergo a strong decrease in the TPR profile of the ZLaMn-2 catalyst, suggesting that they should be associated to phenomena occurring on the support surface which are inhibited by La–Mn oxides dispersion.

The TPR profiles of the supported ZLaMn catalysts show more clearly, with the increase of La–Mn content, the typical features of bulk $LaMnO_3$ giving rise to a multiple signal with a maximum in the 670–700 K range. This signal has been attributed to the reduction of Mn^{4+} (present as 35% fraction in bulk $LaMnO_3$) to Mn^{3+} in analogy to the unsupported catalyst (10, 12). In addition to this peak, a shoulder appears at lower temperature (maximum at about 533 K), more evident for diluted catalysts, as shown in Fig. 4b where the H_2 uptake has been referred to the weight of the active phase (considered as $LaMnO_3$ in the calculation). The ratio between the shoulder and the signals decreases with increasing La–Mn loading, thus suggesting that the first peak could be related to a more easily reducible manganese oxide species. For ZLaMn-2, a further signal appears in the 850–1000 K temperature range, as shown in Fig. 4b. This signal, which cannot be associated to the perovskite phase, indicates that at low loading very stable manganese oxide species are formed on the zirconia surface and strongly interact with the support.

At about 973 K another reduction phenomenon, whose extension increases with perovskite loading, starts for supported samples with a perovskite content ≥12%. In order to better indicate this reduction reaction, a TPR experiment up to 1273 K has been carried out for ZLaMn-16 (not shown). The same reduction process was detected for bulk $LaMnO_3$ and attributed to the further reduction of manganese from a +3 to a +2 oxidation state (10, 12) with the destruction of the perovskite structure. This confirms the formation of perovskite crystallites at higher La–Mn loading, also detected by XRD and inferred by XAS analysis, showing a redox behavior similar to that of unsupported perovskite.

TABLE 2

Results from TPR Experiments[a]

Catalyst	H_2–1073	H_2–850	T_1	T_2
ZLaMn-2	0.43	—	—	1000
ZLaMn-4	0.44	0.40	536	670
ZLaMn-6	0.63	0.54	538	671
ZLaMn-12	0.47	0.38	534	690
ZLaMn-16	0.47	0.33	533	698
$LaMnO_3$	0.59	0.21	—	702

[a] Hydrogen consumption ($mol_{H_2}\ mol_{Mn}^{-1}$) in the range RT-1073 K (H_2-1073), and RT-850 K (H_2-850). Temperatures (K) of the absolute maxima in the range RT-850 (T_1), and in the range 850–1073 (T_2). RT, room temperature.

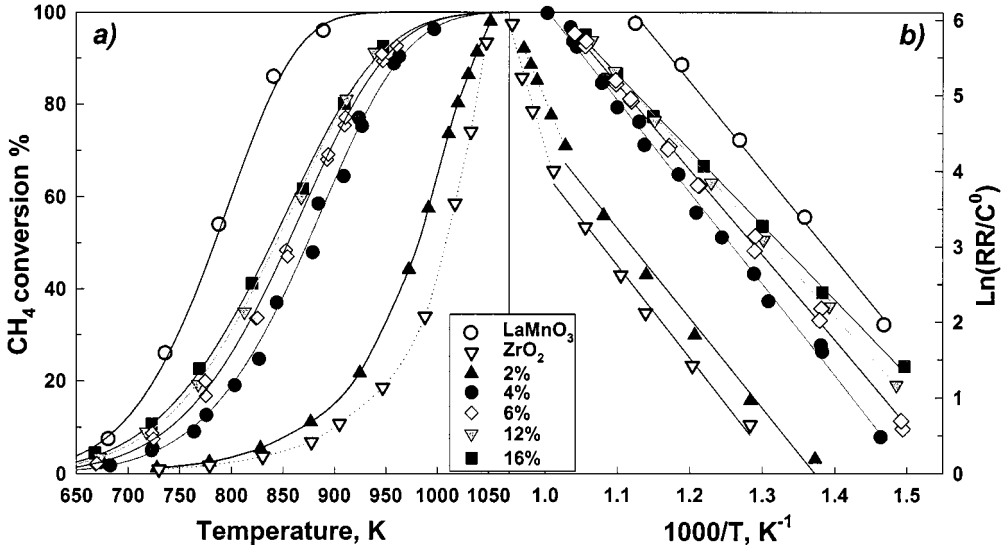

FIG. 5. Methane combustion: (a) CH_4 conversion as a function of the reaction temperature, (b) Arrhenius plot.

Values of the total H_2/Mn ratio estimated for supported La–Mn samples (Table 2) are lower, except for the ZLaMn-6 sample, than those evaluated for bulk $LaMnO_3$, indicating that the pure perovskite undergoes a deeper reduction up to 1073 K. In all the ZLaMn samples but ZLaMn-6 this result could be due to the presence of some Mn^{2+} species or to a partial inhibition of the high temperature reduction process when the active phase is dispersed on the support. On the other hand, the H_2 uptake related to the first peak and associated to the reduction of Mn^{4+}, both in the perovskite and in the oxides, is higher for supported catalysts. This may suggest that the interaction with the zirconia support promotes the formation of Mn^{4+} whose fraction appears to be higher for the ZLaMn-6 catalyst.

3.3. Methane Combustion

Blank tests in the absence of catalyst have been performed under the same reaction conditions of catalytic tests in order to evaluate the contribution of homogeneous reactions. At 973 K 8% of CH_4 is converted with 70% CO_2 selectivity, whereas at 1073 K methane conversion increases up to 45% with about 15% CO_2 selectivity.

The reported reaction rates were not normalized for the surface areas of the samples, because we think that the reported surface area values are mainly attributed to the support, where the supported species are not uniformly spread.

The results of catalytic activity tests of ZLaMn samples and zirconia are reported in Fig. 5a. Supported catalysts with a La–Mn content $\geq$4% activate methane combustion at 723–753 K and give complete CH_4 conversion within 923–973 K, whereas ZLaMn-2 activates the reaction at about 150 K higher temperature, showing poor catalytic performances very close to that of tetragonal ZrO_2. All catalysts with a La–Mn loading $\geq$4% give 100% CO_2 selectivity. On the other hand, tetragonal ZrO_2 and ZLaMn-2 also produce CO both giving a CO_2 selectivity of 15% at 723 K, which increases up to about 50% at 873–923 K. At higher temperatures pure zirconia maintains this selectivity, whereas for ZLaMn-2 a

TABLE 3

Kinetic Parameters for Methane Catalytic Combustion

Catalyst	Ea (kJ mol^{-1})	$A \times 10^{-7}$ (L g^{-1} h^{-1})	T_{50} (K)	CH_4 order (773K)	Reaction rate[a] (mmol g^{-1} h^{-1})	RR_{perov}[a] (mmol g_p^{-1} h^{-1})
ZrO_2	102.0	1.14	1000		0.09	—
ZLaMn-2	99.0	1.25	981		0.16	8.0
ZLaMn-4	100.9	8.79	874	0.79	0.83	20.7
ZLaMn-6	93.8	4.29	855		1.23	20.5
ZLaMn-12	88.8	2.47	844	0.82	1.56	13.0
ZLaMn-16	85.2	1.57	839		1.72	10.8
$LaMnO_3$	97.5	22.7	784	0.83	3.69	3.7

[a] At 773 K, $Y_{CH_4} = 0.4\%$, $Y_{O_2} = 10\%$. RR, reaction rate.

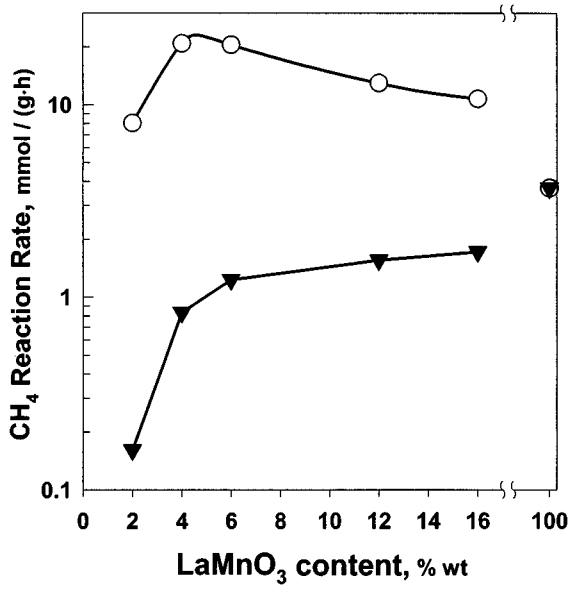

FIG. 6. Methane combustion: reaction rate per gram of catalyst (lower curve) and per gram of perovskite (upper curve) as a function of perovskite loading at 773 K.

decrease of this value to about 15% selectivity at 1043 K is observed.

$LaMnO_3$ apparently has the highest activity, as is also shown by the temperature necessary to give 50% conversion (fourth column of Table 3) and by the value of the reaction rate as evaluated at 773 K and referred to as the total catalyst amount (sixth column of Table 3, triangles in Fig. 6). Nevertheless, based on the reasonable assumption that the active site in the supported samples is in the perovskite or in its active Mn component, we computed the activity of the supported samples and of $LaMnO_3$ per gram of perovskite (last column of Table 3, circles in Fig. 6). In this case the best activity is shown by ZLaMn-4 and ZLaMn-6 which give a value more than five times higher than that of the unsupported perovskite. For La–Mn loading at $\geq$12% the reaction rate starts to decrease slowly, but still remains higher than that of $LaMnO_3$.

In Fig. 5b the Arrhenius plots obtained from the catalytic activity data are reported for pure zirconia, all supported catalysts, and pure $LaMnO_3$. Unsupported perovskite and supported catalysts with a La–Mn content $\geq$4% give rise to plots showing a unique slope, thus suggesting the occurrence of a single kinetic regime in the investigated range of temperature. On the contrary, ZLaMn-2 shows the same behavior of pure zirconia giving rise to Arrhenius plots which can be interpolated by two lines with a different slope. The one at $T > 973$ K is probably related to the occurrence of homogeneous reactions whose contribution becomes non negligible at this temperature for poorly active catalysts. Values of the activation energy (E_a) and preexponential factor (A), estimated from the plots shown in Fig. 5b, are reported in Table 3. All ZLaMn catalysts give rise to Arrhenius plots with a slope quite close to that of $LaMnO_3$ which result in values of E_a ranging from 85 to 101 kJ mol^{-1}. Thus, the interaction with ZrO_2 does not significantly modify the nature of active sites for methane activation, on the contrary to what is frequently reported for alumina-supported perovskites because of the formation of poorly active mixed oxides (16–18). Moreover, catalytic activity measurements at fixed temperature and CH_4 concentrations variable in the range 0.1–1% give an apparent methane reaction order for the supported catalyst very similar to that of bulk $LaMnO_3$ ($n \approx 0.8$, Table 3), probably caused by an inhibition effect related to product adsorption on the active perovskite phase. A weak effect of oxygen

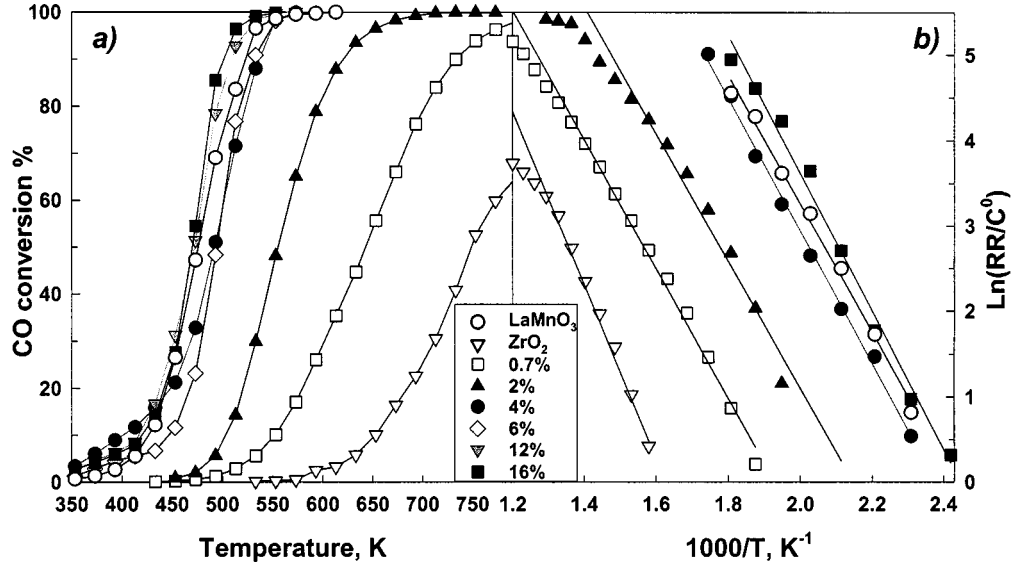

FIG. 7. CO oxidation: (a) CO conversion as a function of the reaction temperature, (b) Arrhenius plot.

TABLE 4

Surface Area (SA) and Kinetic Parameters for CO Catalytic Oxidation

Catalyst	SA ($m^2\ g^{-1}$)	E_a (kJ mol^{-1})	$A \times 10^{-7}$ (L $g^{-1}\ h^{-1}$)	T_{50} (K)	Reaction rate[a] (mmol $g^{-1}\ h^{-1}$)	RR_{perov}[a] (mmol/$g_p^{-1}\ h^{-1}$)
ZrO_2	83	84.5	1.51	749	1.8*e*-3	—
ZLaMn-0.7	55	62.9	0.22	643	0.06	9.13
ZLaMn-2	67	61.9	0.88	556	0.33	16.5
ZLaMn-4	50	64.6	10.6	491	2.00	50.0
ZLaMn-6	55	68.4	25.1	495	1.80	30.1
ZLaMn-12	53	62.3	10.9	472	3.66	30.5
ZLaMn-16	63	67.1	38.3	470	3.82	23.9
$LaMnO_3$	15	62.5	8.85	477	2.85	2.85

[a] At 473 K, $Y_{CO} = 1\%$, $Y_{O_2} = 20\%$.

concentration on the reaction rate is observed, corresponding to an apparent reaction order of 0.15 (O_2 in the range 4–21%, CH_4 0.4%), in agreement with data reported for similar catalysts based on $LaMnO_3$ supported on alumina (18). Such results are in line with a redox mechanism on perovskite-based catalysts, characterized by an intrinsically fast reoxidation step.

In conclusion, the effect of dispersion in ZLaMn-2 leads to the formation of a disordered oxide species with a low activity toward total CH_4 oxidation. For 4–6% loading a maximum dispersion of the active component is reached, resulting in the higher activity per gram of perovskite (circles in Fig. 6). A further loading increase (>6%) results in a particle aggregation of La–Mn oxides with an ensuing decrease of catalytic activity per gram of the perovskite active phase.

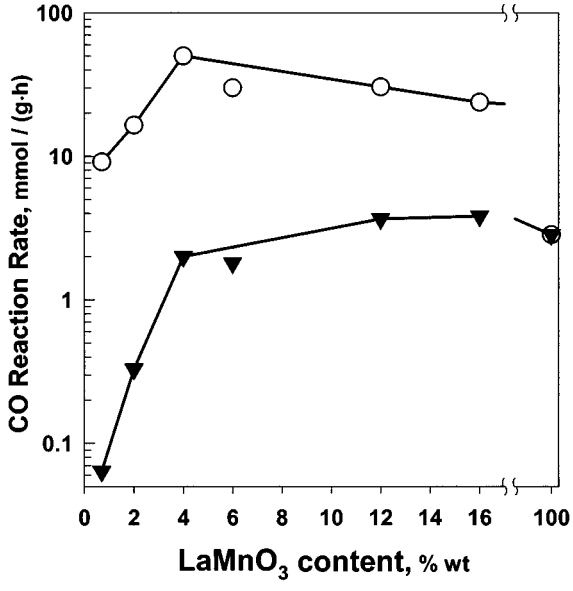

FIG. 8. CO oxidation: reaction rate per gram of catalyst (lower curve) and per gram of perovskite (upper curve) as a function of perovskite loading at 473 K.

3.4. CO Oxidation

The conversion to CO_2 was 100% at $T \leq 800$ K for all catalysts but the pure zirconia support. For the samples with ≥4% loading and for $LaMnO_3$ the conversion reached 100% below 550 K (Fig. 7a).

The apparent activation energy (E_a) for pure zirconia was higher (84.5 kJ mol^{-1}) than that for ZLaMn samples and pure $LaMnO_3$, all showing very similar values in the range from 62 to 68 kJ mol^{-1} (Fig. 7b). The activity of pure zirconia at 573 K on both a weight and a surface area basis was one order of magnitude lower than the most dilute supported catalyst (ZLaMn-0.7). Therefore ZrO_2 is supposed to marginally contribute to the activity of the supported samples, while even very small amounts of the active phase produce a remarkable shift of the conversion values to lower temperatures (Fig. 7a).

In analogy to the results found for methane oxidation, Table 4 and Fig. 8 clearly show that the CO oxidation activities per gram of perovskite of ZLaMn-0.7 and ZLaMn-2 are lower than those for all the other ZLaMn samples, but the pure $LaMnO_3$. This result confirms that in the ZLaMn-0.7 and ZLaMn-2 samples the perovskite structure is not present and metal oxides prevail, whereas in ZLaMn-4 and ZLaMn-6 a perovskite-like phase starts to organize. We suggest that the high oxidation activity is a feature of the perovskite structure, possibly related to the ease of both oxygen adsorption/desorption and the local change of the cation oxidation state.

4. CONCLUSIONS

XRD analysis for the zirconia-supported samples shows only the tetragonal zirconia phase with traces of monoclinic zirconia up to 6% loading. At a higher loading XRD also shows the presence of the perovskite $LaMnO_3$ phase.

XAS analysis confirms the formation of $LaMnO_3$ dispersed on zirconia at high La–Mn loading, whereas at low loading the presence of disordered oxide species strongly interacting with the support is suggested.

TPR experiments indicate the presence of $LaMnO_3$ at high La–Mn loading and La and Mn oxide species at low loading.

The activity trends for methane combustion and CO oxidation appear rather similar. At low La–Mn loading, disordered oxide species strongly interacting with support prevail, and the activity is low, even when calculated at per gram of perovskite. The higher activity of the catalysts with a $\geq$4% loading is related to the incipient formation of a perovskite structure, whose dispersion is maximum at around 4–6%, as demonstrated by the highest rates per gram of perovskite. The analogy of activity–loading trends for the two reactions suggests the similar nature of the active sites operating at a different temperature.

REFERENCES

1. Tejuca, L. G., and Fierro, J. L. G. (Eds.), "Properties and Applications of Perovskite-Type Oxides." Dekker, New York, 1993.
2. Newman, R. E., Navrotsky, A., and Weidner, D. J. (Eds.), *in* "Structure-Property Relationship in Perovskite Electroceramics: Perovskite: A structure of Great Interest to Geophysics and Material Science," p. 66. American Geophysical Union, Washington DC, 1989.
3. Voorhoeve, R. J. H., *in* "Advanced Materials in Catalysis," p. 129. Academic Press, New York, 1977.
4. Garten, R. L., Dalla Betta, R. A., and Schlatter, J. C., *in* "Handbook of Heterogeneous Catalysis" (G. Ertl, H. Knozinger, and J. Weitkamp, Eds.), Vol. 4, p. 1668. VHC Weinheim/New York, 1998.
5. Arai, H., Yamada, T., Eguchi, K., and Seiyama, T., *Appl. Catal.* **26**, 265 (1986).
6. Tejuca, L. G., *J. Less Common Met.* **146**, 261 (1988).
7. Voorhoeve, R. J. H., Johnson, D. W., Jr., Remeika, J. P., and Gallagher, P. K., *Science* **195**, 827 (1977).
8. Tejuca, L. G., Fierro, J. L. G., and Tascón, J. M. D., *Adv. Catal.* **36**, 237 (1989).
9. Delmon, B., and Droguest, J., "Fine Particles," (W. H. Fuhn, Ed.), p. 242. 2nd International Conference, The Electrochemical Society.
10. Lisi, L., Bagnasco, G., Ciambelli, P., De Rossi, S., Porta, P., Russo, G., and Turco, M., *J. Solid State Chem.* **146**, 176 (1999).
11. Porta, P., De Rossi, S., Faticanti, M., Minelli, G., Pettiti, I., Lisi, L., and Turco, M., *J. Solid State Chem.* **146**, 291 (1999).
12. Ciambelli, P., Cimino, S., De Rossi, S., Faticanti, M., Lisi, L., Minelli, G., Pettiti, I., Porta, P., Russo, G., and Turco, M., *Appl. Catal. B Environ.* **24**, 243 (2000).
13. Ciambelli, P., Cimino, S., De Rossi, S., Lisi, L., Minelli, G., Porta, P., and Russo, G., *Appl. Catal. B Environ.* **24**, 243 (2001).
14. Arai, H., and Machida, M., *Appl. Catal. A Gen.* **138**, 161 (1996).
15. Zhang, H. M., Teraoka, Y., and Yamazoe, N., *Appl. Catal.* **41**, 137 (1988).
16. De Collongue, B., Garbowski, E., and Primet, M., *Chem. Soc., Faraday Trans.* **87**, 2493 (1991).
17. Zwinkels, M., Haussner, O., Jaras, S., and Menon, P., *Catal. Today* **47**, 11 (1999).
18. Cimino, S., Pirone, R., Lisi, L., Turco, M., and Russo, G., *Catal. Today* **59**, 19 (2000).
19. Fuji, H., Mizuno, N., and Misono, M., *Chem. Lett.* 2147 (1987).
20. Mizuno, N., Fujii, H., Igarashi, H., and Misono, M., *J. Am. Chem. Soc.* **114**, 7151 (1992).
21. Chuah, G. K., Janice, S., Cheong, S. A., and Chan, K. S., *Appl. Catal. A Gen.* **145**, 267 (1996).
22. Ankudinov, A. L., Ravel, B., Rehr, J. J., and Conradson, S. D., *Phys. Rev. B* **58**, 7565 (1998).